



High thermal stability of RF dielectric properties of BiVO₄ matrix with added ZnO

R. G. M. Oliveira² · D. C. Souza³ · J. E. V. de Morais^{1,2} · G. S. Batista² · M. A. S. Silva² · D. X. Gouveia³ · S. Trukhanov^{4,5,6} · A. Trukhanov^{4,5,6} · L. Panina^{4,7} · C. Singh⁸ · D. Zhou⁹ · A. S. B. Sombra^{1,2}

Received: 26 March 2020 / Accepted: 22 June 2020 / Published online: 7 July 2020
© Springer Science+Business Media, LLC, part of Springer Nature 2020

Abstract

In this work, a complex impedance spectroscopy study of bismuth vanadate (BiVO₄) ceramics with different additions of ZnO (25, 50, and 75 wt %) was performed. BiVO₄ (BVO) was synthesized by the reaction method in solid-state and calcined at 500 °C and BVO–ZnO composites were moulded in sintered ceramic pellets at 700 °C. X-ray diffraction (XRD) was used to analyse the crystal structure of BVO and the BVO–ZnO composites; none spurious phase was observed during the synthesis. Analysis by complex impedance spectroscopy (CIS) showed that increasing the concentration of ZnO reveals increased activation energy due to thermo-activated charge transfer for the sample with 25 wt % ZnO. At room temperature, the increase in the ZnO concentration in the BVO matrix maintained a high value for the dielectric constant (ϵ), in the order of 10^4 at a frequency of 1 Hz. Average normalized change (ANC) was used to identify the temperature at which the available density of trapped charge states vanishes in each sample. The temperature coefficient of capacitance was positive for BVO and negative for composites. The adjustment through the equivalent circuit presented excellent electrical response for the composites, and identified an association with three resistors, each in parallel a constant phase element, showing the influence of grain and grain boundary on the process of thermo-active conduction.

✉ A. S. B. Sombra
asbsombra@gmail.com

R. G. M. Oliveira
ronaldomaia@fisica.ufc.br

D. C. Souza
dougsoza1902@gmail.com

J. E. V. de Morais
eduardovasconc@gmail.com

G. S. Batista
graciliano@fisica.ufc.br

M. A. S. Silva
marceloassilva@yahoo.com.br

D. X. Gouveia
dxgouveia@gmail.com

S. Trukhanov
sv_trukhanov@mail.ru

A. Trukhanov
trukanov86@mail.ru

L. Panina
drlpanina@gmail.com

C. Singh
rcharanjeet@gmail.com

D. Zhou
zhoudi1220@gmail.com

- ¹ Telecommunication Engineering Department, Federal University of Ceará (UFC), P.O. Box 6007, Fortaleza, Ceará 60755-640, Brazil
- ² Telecommunication and Materials Science and Engineering Laboratory (LOCEM), Physics Department, Federal University of Ceará (UFC), Pici Campus, P.O. Box 6030, Fortaleza, Ceará 60455-760, Brazil
- ³ Federal Institute of Ceará, Fortaleza/IFCE Campus, Fortaleza, Ceará 63400-000, Brazil
- ⁴ National University of Science and Technology (MISiS), Leninskii Av., 4, Moscow, Russia 4119049
- ⁵ South Ural State University, Lenin Av., 76, Chelyabinsk, Russia 454080
- ⁶ Scientific and Practical Materials Research Center of the NAS of Belarus, P. Brovki Str., 19, Minsk 220072, Belarus
- ⁷ Institute of Physics, Mathematics & IT, Immanuel Kant Baltic Federal University, A. Nevskiy Str., 14, Kaliningrad, Russia 236041
- ⁸ School of Electronics and Electrical Engineering, Lovely Professional University, Phagwara, India
- ⁹ Electronic Materials Research Laboratory, Key Laboratory of the Ministry of Education & International Center for Dielectric Research, School of Electronic Science and Engineering, Xi'an Jiaotong University, Xi'an 710049, China

1 Introduction

Electrical components that have physical properties which tend towards stable values during a change of temperature—such as conductivity, dielectric constant, and losses—are of great interest for industrial applications. Works in the literature show the dielectric studies some of the BVO-composites under variations in temperature directed in the microwave range [1–6]. Composite materials are a class of materials that are composed of materials of different physical and chemical characteristics which can result in interesting properties, such as permittivity, dielectric loss factor, and others with specific applications [7]. Thus, by mixing materials with different stoichiometric properties and with certain properties, it is possible to produce ceramic phases that at the same time exhibit a variety of crystals, structures, and inclination systems, presenting parameters that are governed by the charge, size of the ions, and electronic configuration. The ordered state is established by the difference in ions, as well as the difference in ionic rays, so the relationship between dielectric properties and conductivity explains understanding composites with a high dielectric constant (ϵ), low dielectric loss ($\tan \delta$), temperature capacitance coefficient (TCC) as close to zero as possible, and sintering temperature below 800 °C; there have been recent significant developments in electroceramics associated with radiofrequency (RF) and microwave telecommunications that have given rise to low material temperature co-fired ceramics (LTCC) which are applied in circuits whose passive components (resistors, capacitors, and inductors) are used in the structure of active integrated circuits [8] and photocatalytic oxidation [9].

Vanadium pentoxide-based dielectric ceramics (V_2O_5) are suitable for LTCC [10–12]; when associated with bismuth oxide (Bi_2O_3), there is a change of state at approximately 817 °C. Monoclinic $BiVO_4$ (BVO) may have photocatalytic, ferroelastic, and dielectric properties, for use in pigments and application in devices that operate in RF, such as high-performance capacitors [10, 12–14].

BVO (space group I2/b) presents a reversible phase transition at 255 °C correspondent the change ferroelastic (monoclinic) to paraelastic (tetragonal scheelite) symmetry and an irreversible transition the phase monoclinic for the tetragonal zircon-type between 400–500 °C [15].

When prepared using a sol–gel method at room temperature, BVO presents great photocatalytic activity [16], when compared with conventional solid-state reaction synthesis [2]. In the low-temperature co-fired ceramics (LTCC) fabrication, the BVO is generally used as a sintering aid [17, 18].

In the search for more material options that could be used with BVO, without affecting its properties, at a lower sintering temperature and shorter grinding time, zinc oxide (ZnO)

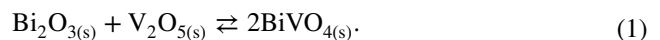
presents itself as a good candidate to form a composite with BVO because of its relatively high conductivity [19], a low value of activation energy, high dielectric constant at room temperature, and properties close to that of BVO [20].

The ZnO, when sintered at 1300 °C, presents in RF ϵ of 3.70×10^5 , an $E_a = 0.19$ eV, relative density of approximately 92%, and TCC goes from a negative to a positive value between the frequency of 10 Hz and 10 kHz. Microwaves have a ϵ of 12.8, $\tan \delta$ of 1.41×10^{-2} , and a temperature coefficient of resonant frequency (τ_f) of 70.79 ppm °C⁻¹ [20].

In an endeavour to find thermo-stable materials and LTCC in the RF range, this work used the composite formed by the ceramic phases BVO–ZnO. The structural phase of BVO and ZnO was studied using X-ray diffraction (XRD), complex impedance spectroscopy (CIS) for dielectric study at a frequency range of 1 Hz to 1 MHz, and temperature variation (room temperature, and 300 °C to 460 °C). In the electric study, some parameters as the temperature coefficient of capacitance (TCC), activation energy (E_a), conductivity (σ), dielectric permittivity (ϵ), and dielectric loss ($\tan \delta$) were analyzed. Also was used an equivalent circuit fitting to it and analyze the electrical internal (bulk) and external (grain boundary, surface layer, and electrode) contributions for BVO and BVO–ZnO samples [21–24].

2 Experimental procedure

A stoichiometry appropriate was used for the preparation of BVO according to Eq. 1 applying the conventional solid-state reaction method. The synthesis process was made using the commercial oxides V_2O_5 of Aldrich with 99% purity and Bi_2O_3 of Vetec with 98% purity, for the synthesis of BVO, and ZnO of Vetec with 99.9% purity was used in the formulation of BVO–ZnO composites.



The samples were manufactured through by mixing of BVO and ZnO, varying ZnO concentration from 0 to 75%wt; mixtures named BVO, BVZ25, BVZ50, and BVZ75 had a concentration of 0, 25, 50, and 75% wt ZnO, respectively, to make up the BVO–ZnO mixtures.

Through planetary mills, the stoichiometric proportions of Bi_2O_3 and V_2O_5 were ground in a polyacetal jar using zirconia balls for 6 h. The same mixing process was adopted for samples with added ZnO, which were sintered at 700 °C for 4 h. The sintered BVO and BVZ powders were subjected to heating/cooling rates of 0.5°/min. Powders were subsequently examined at room temperature using $CuK\alpha$ radiation ($\lambda = 1.540562$ Å) in a Rigaku $K\alpha$ diffractometer over an angular range of ($20^\circ \leq 2\theta \leq 80^\circ$). The phases of the BVO and BVZ ceramic obtained by calcination and sintering

processes were identified through Rietveld refinement by analysing their diffraction peaks and confirming the proposed crystalline phases.

A hydraulic press at a constant uniaxial pressure of 98 MPa was used for the production of pellets from BVO powder and BVO–ZnO composites. In this process, polyvinyl alcohol (PVA) was used as a binder to reduce the brittleness of the pellets. A sintering process at 700 °C for 4 h in an air atmosphere, with an intermediate step of 500 °C for 2 h, was used to eliminate organic binder. For the best electrical contact, after sintered, all samples pellets were polished and painted with conductive paint.

The verification of the dielectric parameters was realized through a computer-controlled impedance analyzer (Solartron 1260), operating in the frequency range (1 Hz–1 MHz) and temperature ranging from 300 to 460 °C.

3 Results and discussion

To identify the phase present in the BVO, the sample was analysed using an X-ray diffraction technique (XRD). The least squared method was applied to the experimental data, which constitutes the Rietveld method, where the profiles were compared with the standard phase of the structure of the inorganic crystals database (ICSD) 100604; the experimental pattern is shown in Fig. 1. In Fig. 1, the difference between the calculated intensity and the observed intensity represents the residue, which is a small value. Plan 112 shows the main peak of BVO and other plans show peaks that identify the BVO, without any major purity phase [25].

In Rietveld refinement, the DBWS9807 program was used and the graphical interface provided by Bleicher et al.

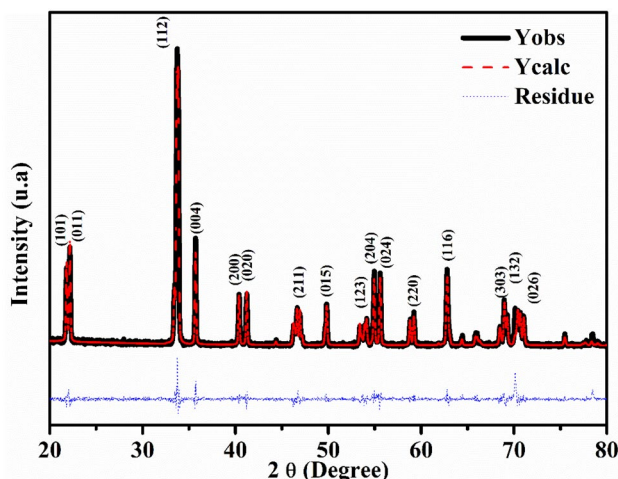


Fig. 1 Powder diffraction pattern of BiVO_4 , observed and calculated intensity

Table 1 Rietveld refinement data for the BVO sample patterns obtained from X-ray diffraction

Parameters structural					
a	5.1956	b	5.0935	c	11.7045
α	90.0	β	900	γ	90.383
Density (g/cm^3)	6.955	Mass (%)	100.0	Molar (%)	100.0
$R\text{-P}$ (%)	12.76	$R\text{-WP}$ (%)	18.49	$R\text{-expected}$	16.76

[26] was used to obtain refinement parameters. The studied (BiVO_4) matrix presents a monoclinic structure (space group $I2/b$) proven by experimental diffractogram the single-phase; the good agreement between the parameters observed and calculated showed that the refinement was efficient because it was not identifying any trace of extra peaks. Table 1 lists the refinement results with the parameter controls which are consistent with the reported results [27, 28].

Figure 2 shows powder XRD patterns of BVO, BVZ25, BVZ50, and BVZ75 at room temperature. This analysis was performed to investigate the phases in the samples and better understand the dielectric and electric behaviour of these fabricated ceramics.

No secondary phases were observed for patterns obtained for pure BVO and BVO–ZnO. From the results shown in Fig. 2, one can see how the intensity of the main peaks of BVO and ZnO evolve with increasing ZnO concentration. The Rietveld refinement performed on composites shows that the parameters obtained led to the identification of only two crystalline phases, BVO and ZnO, and all values of R_{Bragg} , S , and R_{wp} are in agreement with the acceptable refinement proposed in the literature [29, 30]. The values of the residual parameters of refinement are listed in Table 2, which shows the R_{wp} is a merit parameter (the lower its value, the better the diffractogram calculated by DBWS) and must be between 10 and 20;

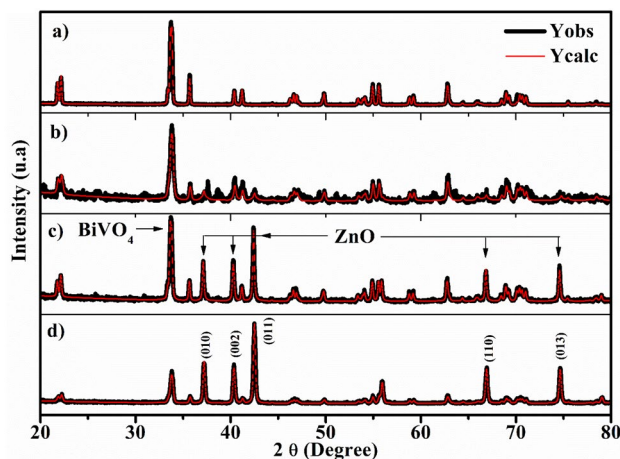


Fig. 2 XRD of sintered samples at 700 °C/4 h: **a** BVO (ICSD-100604), **b** BVZ25, **c** BVZ50, and **d** BVZ75

Table 2 Rietveld refinement data for the BVO–BVZ sample patterns obtained from X-ray diffraction

Sample	Parameters			Density (g/cm ³)		Relative density (%)
	<i>S</i>	<i>R</i> _{wp}	Bragg <i>R</i> -Factor	Theoretical	Experimental	
BVO	1.05	18.49	5.43	6.95	6.52	93.8
BVZ25	1.12	18.96	7.42	6.63	4.04	60.9
BVZ50	0.99	20.39	4.81	6.20	4.15	66.9
BVZ75	0.99	18.81	2.57	5.88	3.99	67.8

the *S* (goodness-of-fit) parameters were all below 1.5, while the *R* Bragg, which is used in the indication of the models for each phase and is influenced by instrumental and structural parameters, were all below 9%. Hence, the phase proposed for refinement is in accordance with the experiment results [31].

It is possible to observe that the addition of ZnO caused a decrease in the relative density value (Table 2), probably due to the low sintering temperature of the samples, since better densification of pure ZnO requires a higher temperature, but the samples remained with high mechanical resistance. However, it is noticeable that the increase in ZnO in the matrix increases the relative density of the compound, making this addition promising.

The complex impedance spectroscopy (CIS) method was used to analyse the electrical and dielectric properties (impedance, conductivity, dielectric constant, losses, and activation energy) of the samples studied [32], using the frequency range 1 Hz to 1 MHz with temperature ranging from 300 °C to 460 °C. Dielectric properties can be expressed as a function of the complexes of impedance (Z^*), electric modulus (M^*), and dielectric constant (ϵ^*) and expressed mathematically as follows:

$$Z^* = Z' - jZ''; \quad M^* = 1/\epsilon^*(\omega) = j(\omega C_0); \quad Z^* = M' - jM'',$$

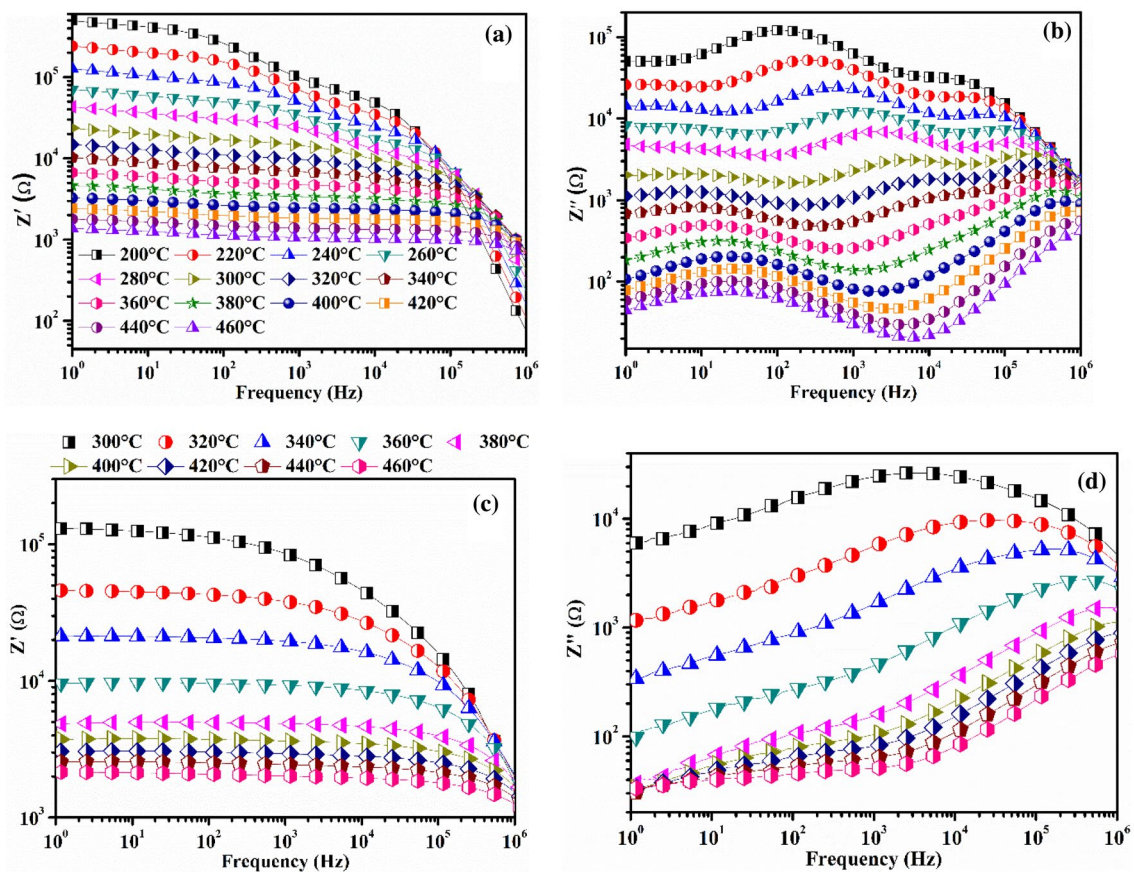


Fig. 3 Dependence of the real and imaginary parts of the impedance with frequency at different temperatures for **a** Z' (BVO), **b** Z'' (BVO), **c** Z' (BVZ25) and **d** Z'' (BVZ25)

where (Z' , M') and (Z'' , M'') are the real and imaginary components of impedance and module, respectively. ω is the angular frequency ($\omega = 2\pi f$), and the imaginary number $j = \sqrt{-1}$ [33]. Figure 3a, c displays the results of real impedance values and Fig. 3b, d shows imaginary impedance for BVO and BVZ25, respectively. As the temperature increases, a region that is increasingly independent of the frequency is observed; this region in Fig. 3a ranges from 1 Hz to 2×10^5 Hz. After this region in the high-frequency domain, there is a decrease in the energy barrier with separation of charge carriers in the materials, while in Fig. 3c, with the addition of ZnO, there is a predominant polarization effect, as the temperature increases with increasing frequency, the dipoles are no longer able to follow the electric field, causing an independent region frequency in a range from 1 Hz to 4×10^5 Hz. Thus, there is a decrease in the energy barrier due to the release of space charges.

Table 3 Values of Z' , Z'' , ϵ and σ_{dc} for all samples at 1 Hz

	BVO	BVZ25	BVZ50	BVZ75
Room temperature				
Z' (Ω)	2.61×10^4	5.78×10^5	2.68×10^5	3.37×10^5
Z'' (Ω)	3.69×10^4	2.73×10^4	1.94×10^4	2.48×10^4
ϵ	2.61×10^4	1.53×10^4	5.06×10^4	4.09×10^4
σ_{dc} ($\Omega \text{ m}$) ⁻¹	1.57×10^{-5}	1.81×10^{-5}	3.89×10^{-5}	3.09×10^{-5}
300 °C				
Z' (Ω)	4.95×10^5	1.33×10^4	6.59×10^4	5.28×10^4
Z'' (Ω)	5.02×10^4	5.83×10^3	3.22×10^3	2.67×10^3
ϵ	4.13×10^5	6.38×10^4	1.39×10^5	1.80×10^5
σ_{dc} ($\Omega \text{ m}$) ⁻¹	1.27×10^{-5}	7.98×10^{-5}	1.58×10^{-4}	1.98×10^{-4}
460 °C				
Z' (Ω)	1.36×10^3	2.14×10^3	8.98×10^3	3.88×10^4
Z'' (Ω)	4.40×10^1	3.19×10^1	6.06×10^2	4.36×10^2
ϵ	2.71×10^6	1.30×10^6	1.41×10^6	8.27×10^5
σ_{dc} ($\Omega \text{ m}$) ⁻¹	4.67×10^{-3}	4.98×10^{-3}	1.16×10^{-4}	1.05×10^{-4}

Figure 3b, d shows the imaginary impedance of the pure sample and the sample with added ZnO. These graphs are suitable for the evaluation of the relaxation frequency of most of the RF resistive components. In these curves, we have highlighted the appearance of peaks that move towards values of the greater frequency with increasing temperature; consequently, Z' decreases with increasing temperature. In Fig. 3b, we have two peaks: the first is located at the frequency of 20 Hz and the second at the frequency of 200 Hz. Both are quite wide and there is dispersion with increasing temperature, as shown in Fig. 3d, peaking at the frequency of 300 Hz at 300 °C which moves to high frequencies.

A thermo-activated process was revealed in the Z'' spectra due to the displacement of the peak present in these spectra. This processes can be due to the dipole reorientation, profile of high dielectric constant (ϵ) systems, as shown in Table 3 [34], and conduction electronics due to grains (bulk), grain boundary, and interface effects for BVO samples and grain (bulk) for BVZ25–BVZ75.

Table 3 shows that the variation of Z' and Z'' at 1 Hz can be explained because of the dielectric properties of the ZnO [20], probably because of variation in reduction of space charge polarization, with the respective increase in frequency in the material [35].

Figure 4 shows the conductivity (σ) and its correlation with the frequency and the dependence on temperature. This phenomenon (σ) is generally analysed using Jonscher's law [36–38]. The Arrhenius relation $f = f_0 \exp[-E_a/kT]$ or $\sigma = \sigma_0 \exp[-E_a/kT]$, where T is absolute temperature, k is the Boltzmann constant and E_a is the activation energy related to the conduction process. This relation is appropriate because it can explain thermo-activated processes shown in the results of the conductivity spectra and imaginary electric modulus (M'').

Figure 5 shows the behaviour of the mobility of charge carriers in the BVO and BVZ25 samples through average normalized change (ANC), which compares the changes

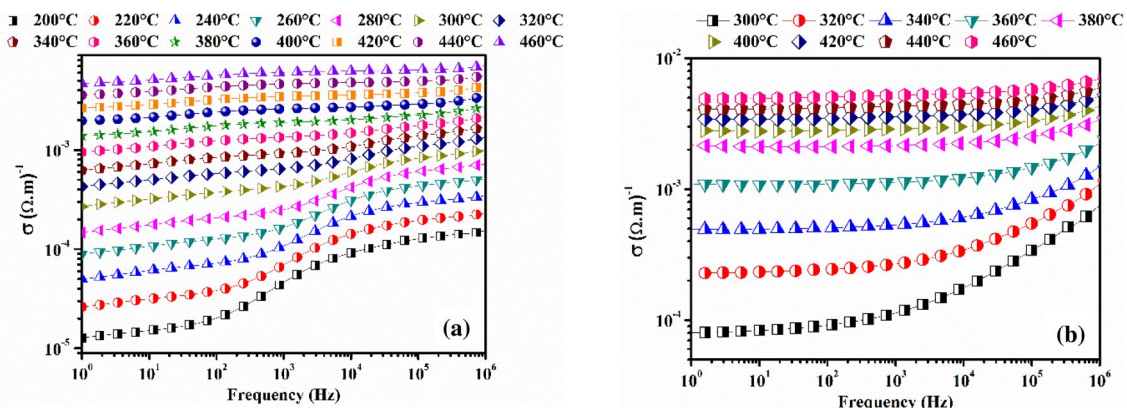


Fig. 4 Real conductivity with frequency at various temperatures for **a** BVO and **b** BVZ25

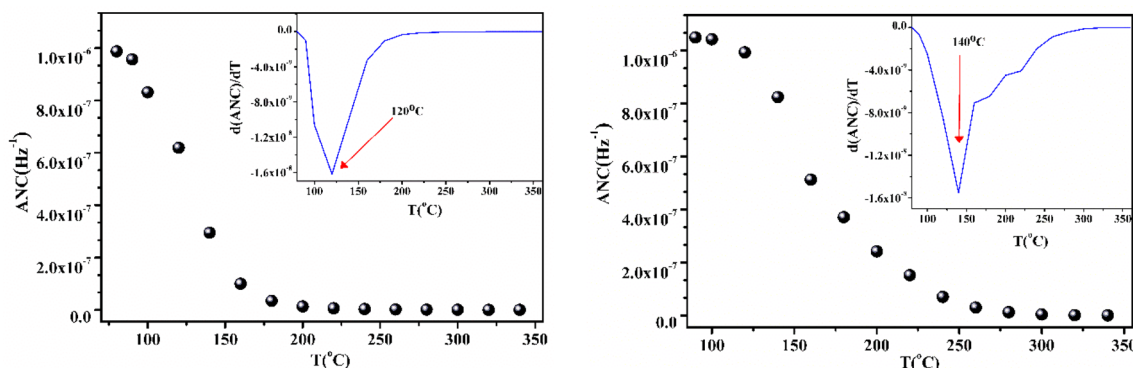


Fig. 5 Temperature dependence of ANC for the composites a BVO and b BVZ25; the inserted graph is the rate of change of ANC with temperature

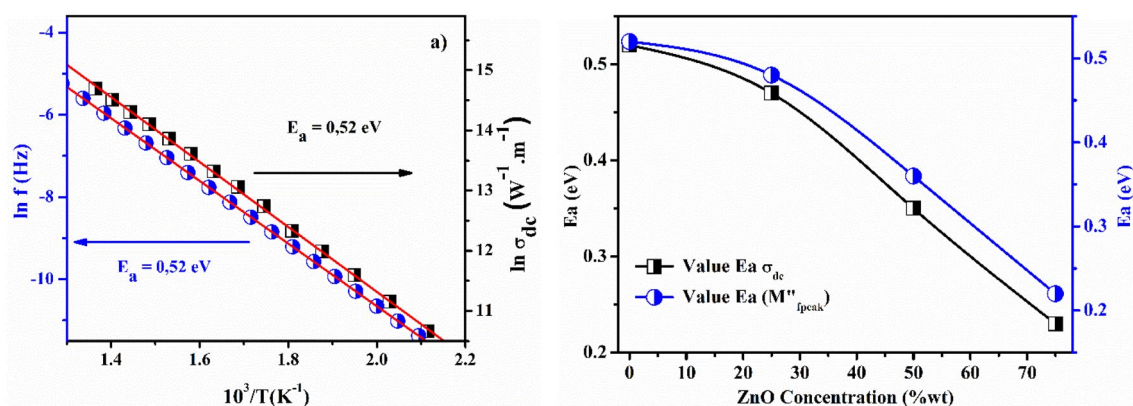


Fig. 6 Arrhenius plots for a BVO and b all samples with dependence of σ_{dc} and f_{max} (peak) vs $1000/T$

observed in the variation of the real part of impedance (Z') against frequency at different temperatures. ANC is considered to be the intrinsic response of the material and calculated by the relation $(\Delta Z'/\Delta f)/Z'_0$ to all temperatures, where $\Delta Z' = Z'_{low} - Z'_{high}$ and $\Delta f = f_{low} - f_{high}$. The terms of impedance Z'_{low} and Z'_{high} are the Z' values at low and high frequency (f), respectively. Z'_0 is the value of the real part of impedance extracted from the low-frequency limit by extrapolation of Z' at each temperature.

According to both graphs, a low-temperature region is observed; ANC values are less temperature-dependent around 10^{-6} Hz^{-1} . Then, the ANC decreases until it reaches the value of 1.3×10^{-8} at 200°C and at 280°C in the curves of BVO and BVZ25, respectively; after this, the ANC is temperature independent for increasing temperature. These changes indicate different conduction mechanisms for different temperature regions [39, 40]. The insets in Fig. 5a, b represent the temperature dependence of the rate of change for ANC. The slope shows information about the correspondent temperature to the density number of trapped charges released. When the derivative of the ANC reaches

Table 4 Activation energies for the BVO–ZnO samples and RF at room temperature, ϵ , and $\tan \delta$

Data source	BVO	BVZ25	BVZ50	BVZ75
Activation energy (eV)				
Modulus spectrum	0.52 eV	0.48 eV	0.36 eV	0.22 eV
DC conductivity	0.52 eV	0.47 eV	0.35 eV	0.23 eV
Dielectric measurements in RF at 100 Hz				
ϵ (100 Hz)	3.18×10^2	3.21×10^2	4.91×10^2	3.36×10^2
$\tan \delta$ (100 Hz)	1.04×10^1	1.11×10^1	1.55×10^1	1.81×10^1

a minimum value, the available density of trapped charges vanishes. Such effects are observed in the BVO and BVZ25 samples at 120°C and 140°C , respectively. That behaviour confirms the presence of different conduction mechanisms.

To calculate the activation energies of each sample, the DC conductivity at 1 Hz and the peak frequency of the electric module (f_{peak}) were used.

The increase in ZnO concentration causes an increase in conductivity, as listed in Table 3 and Fig. 4a, b.

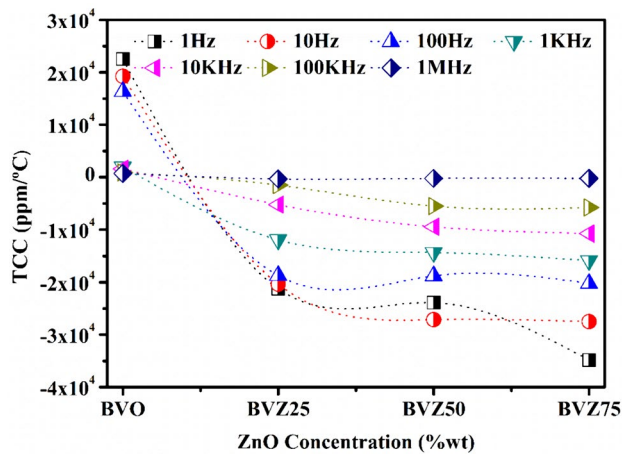


Fig. 7 Capacitance variation with temperature (TCC) for all samples

At low frequency and temperature, all samples feature points of constant conductivity with frequency, related to a DC conductivity, so, the increase in added ZnO caused a slight increase in conductivity values.

Figure 6 and Table 4 show the values of the activation energy, measured from conductivity and frequency relaxation of the M'' , standing out small variations in values compared with other works in the literature [41, 42], indicating that the electrical properties responsible for the relaxation process and electrical conduction is the same, and it's still noticeable by the angular coefficient (Fig. 6a), a trend towards the same thermal activation process [43–47].

This behaviour can be explained by the low value of E_a for ZnO [20] compared with BVO [12, 48] and vacancies in BVO resulting from sinterization, so, the E_a values obtained, are associated with the thermal-activated process, on account the values conductivity and shift of relaxation frequency are close.

The temperature coefficient of capacitance (TCC) is another important parameter in electronic engineering applications and RF components [49]; as long as this value is

near zero, it can be applied as a component in circuits due to thermal stability.

From Fig. 7 and as confirmed in Table 5, it can be seen that TCC is not affected by a concentration of ZnO located between BVO and BVZ25, wherein TCC changes from positive to negative with ZnO addition, indicating that in this region there will be a range of concentrations that will present thermal stability: that is, there will be no variation of its dielectric properties with temperature variation. Knowing that a capacitor efficient cannot receive external influence, as temperature variation, because this affects the dielectric or electric properties, we have that the BVO–ZnO composite can be used to manufacture this type of component, because of its thermal stability.

One way to identify the electric contribution of grain and grain boundary is from a Nyquist diagram and an equivalent circuit using experimental results. The equivalent circuit models studied here were identified by combining constant phase elements (CPE) and resistances (R), these elements being interconnected, in series or in parallel combinations for adjustment and understanding the experimental data and understand the electric response of the grain and grain boundary.

The identification of the different electric relaxations caused by the grain, grain boundary, and electrode effects of the ceramic materials was carried out through an impedance analysis [23]. These types of relaxation at low temperatures and in low- and high-frequency regions are shown in Fig. 8 [50].

By the experimental dataset, it is possible to represent impedance complex plane through the Nyquist plots, where the electrical response of grain, grain boundary, and electrode effect in ceramic materials can be observed through the CIS [51].

Figure 8 shows the plots which represent the impedance measurements made at room temperature for samples BVO and BVZ from 300 to 460 °C, where each semicircle may represent a single relaxation mechanism associated with the microstructure of electroceramics and that can be fitted from an equivalent circuit [52–54] being that at the highest frequencies the semicircle is associated with the grain (R_1 –CPE $_1$), the second arc is associated with the

Table 5 TCC values for all samples

Frequency	BVO	BVZ25	BVZ50	BVZ75
$f=1$ Hz (TCC (ppm/ °C))	22,506.10	– 21,216.40	– 23,897.89	– 34,844.84
$f=10$ Hz (TCC (ppm/ °C))	19,264.27	– 20,362.67	– 27,122.27	– 27,486.13
$f=100$ Hz (TCC (ppm/ °C))	16,346.54	– 18,687.00	– 18,781.29	– 20,226.06
$f=1$ kHz (TCC (ppm/ °C))	1968.85	– 11,918.35	– 14,329.56	– 15,872.09
$f=10$ kHz (TCC (ppm/ °C))	1602.16	– 5243.36	– 9469.31	– 10,746.68
$f=100$ kHz (TCC (ppm/ °C))	891.78	– 1521.90	– 5513.97	– 5791.16
$f=1$ MHz (TCC (ppm/ °C))	704.22	– 325.35	– 240.11	– 222.05

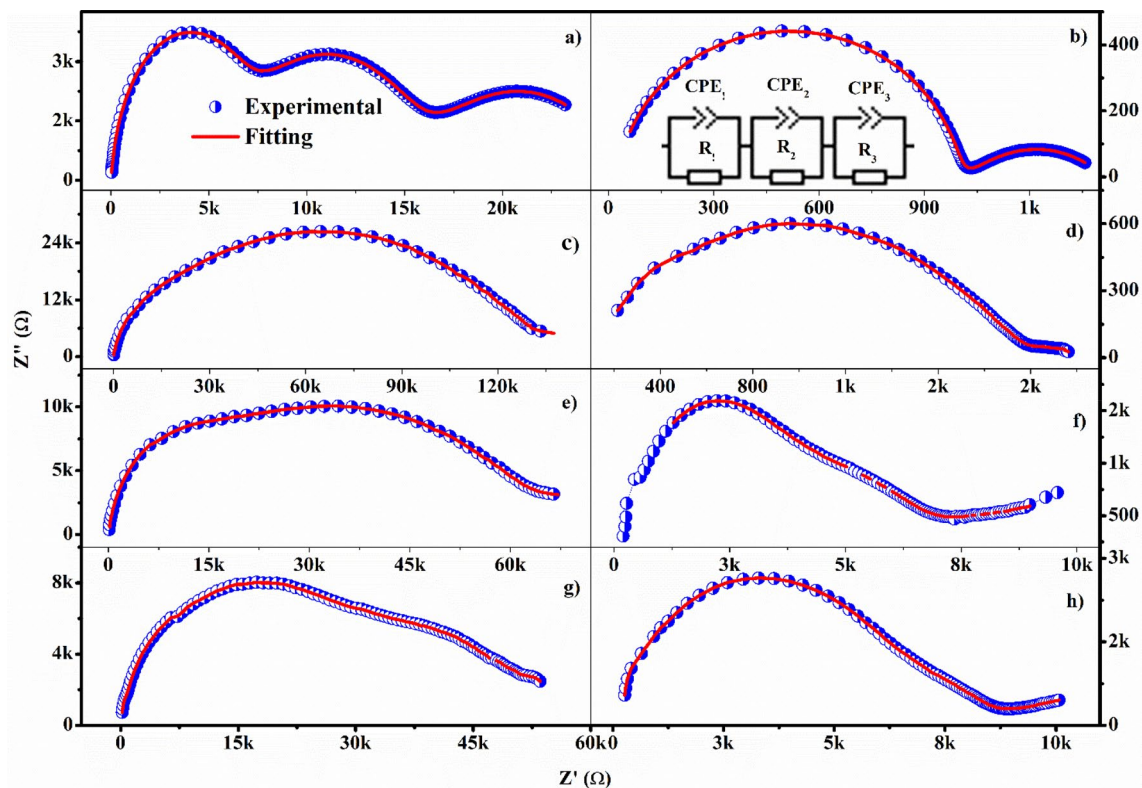


Fig. 8 Nyquist plot additions of BVO and BVZ25 with an electrical equivalent circuit for 300 °C and 460 °C, respectively: **a, b** (BVO), **c, d** (BVZ25), **e, f** (BVZ50), and **g, h** (BVZ75)

Table 6 Fit of equivalent circuit parameters for BVO, BVZ25, BVZ50, and BVZ75 with temperatures of 300 °C and 460 °C, respectively

Sample	Grain			Grain boundary			Electrode effect		
	R_1 (kΩ)	P_1	n_1	R_2 (kΩ)	P_2	n_2	R_3 (kΩ)	P_3	n_3
300 °C									
BVO	914	2.4×10^{-9}	0.708	352	6.8×10^{-6}	0.383	602	5.0×10^{-4}	0.803
BVZ25	94.2	1.6×10^{-9}	0.797	27.7	4.4×10^{-8}	0.574	23.1	1.2×10^{-5}	0.370
BVZ50	37.5	1.3×10^{-7}	0.540	14.7	8.7×10^{-10}	0.818	18.0	8.6×10^{-6}	0.387
BVZ75	29.3	2.5×10^{-6}	0.370	7.76	4.3×10^{-10}	0.870	18.7	2.4×10^{-8}	0.640
460 °C									
BVZ25	0.79	1.5×10^{-10}	0.946	0.27	9.8×10^{-5}	0.218	1.17	2.2×10^{-9}	0.978
BVZ50	5.62	9.1×10^{-5}	0.243	3.08	2.2×10^{-7}	0.597	2.67	4.0×10^{-10}	0.867
BVZ75	10.5	4.7×10^{-4}	0.232	3.63	5.3×10^{-7}	0.483	5.01	7.9×10^{-11}	0.929

R resistance, P , and N are parameters of the CPE element circuit

grain boundary (R_2 -CPE₂), and the third semicircle in the low-frequency range is associated with the electrode effect (R_3 -CPE₃) [33].

The fitted values are shown in Table 6, where R and CPE (P and n parameters, where P is a factor of proportionality and n is the CPE exponent that characterizes the phase shift) represent the experimental results obtained by an equivalent circuit model formed by three associations of R -CPE; in these results, fitted values were observed

to depend on the temperatures and composition of the sample.

The influence of ZnO in the ceramic BVO matrix can be seen in Fig. 8 and compared in Table 6. For the BVO-ZnO blend, it is noticeable that the fit includes three components of the electric process (grain, grain boundaries and electrode effect).

The increase in ZnO concentration causes a sharp decrease in resistivity, indicating an increase in conductivity for compositions at 300 °C.

Despite the sharp drop in resistance in all samples with added ZnO in relation to BVO, the BVZ50 composition showed a slight increase in its resistance for all temperatures analysed.

4 Conclusion

This work has successfully completed the study of structural and dielectric characteristics of the pure phase of BiVO₄ and ZnO additions. (25, 50, and 75 wt %). Obtained by solid-state reaction and with low sinterization temperature (800 °C), BVO can be considered a ceramic with LTCC due to a low calcination temperature (500 °C). The added samples of ZnO presented a thermo-activated process with an E_a value of around 0.22–0.48 eV. It was observed a dielectric relaxation for all samples at room temperature from ϵ and $\tan \delta$ spectra. For the BVZ50 in 100 Hz, the ϵ is close to 500 and a dielectric loss of 10^1 . The ANC behaviour at different temperatures showed that the addition of 25 wt % ZnO in a BVO matrix increases the temperature at which the available density of trapped charge states vanishes. The experimental measurements show the inversion of TCC values, where the signal of TCC goes from positive to negative, indicating that the material in this concentration range has thermal stability and is thus appropriate for applications in circuits and components that work in RF. The Nyquist diagram with semicircle arcs present, were modelled by three associations of R–CPE, representing an equivalent circuit and characterizing the impedance spectrum, implying appropriateness for use in electronic circuits.

Acknowledgements The authors are grateful to CNPq (402045/2013-0), the US Air Force Office of Scientific Research (AFOSR) (FA9550-16-1-0127), and CNPq (Process: 402561/2007-4, Edict MCT/CNPq n° 10/2007) for providing financial support and to the X-Ray Laboratory of the Federal University of Ceará for XRD analysis.

References

- L. Hoffart, U. Heider, R.A. Huggins, W. Witschel, R. Jooss, A. Lentz, *Ionics* **2**, 34 (1996)
- F. Gu, G. Chen, X. Kang, X. Li, C. Zhou, C. Yuan, Y. Yang, T. Yang, *J. Mater. Sci.* **50**, 1295 (2015)
- D. Zhou, L.-X. Pang, H. Wang, J. Guo, X. Yao, C.A. Randall, *J. Mater. Chem.* **21**, 18412 (2011)
- M.I.M.T. Abdullah, A. Halim, N.M. Ali, *Malays. J. Anal. Sci.* **13**, 151 (2009)
- R.G.M. Oliveira, J.E.V. de Morais, G.S. Batista, M.A.S. Silva, J.C. Goes, A.S.B. Sombra, *J. Alloys Compd.* **775**, 889 (2019)
- R.G.M. Oliveira, R.A. Silva, J.E.V. de Morais, G.S. Batista, M.A.S. Silva, J.C. Goes, H.D. de Andrade, I.S. Queiroz Júnior, C. Singh, A.S.B. Sombra, *Composites B* **175**, 107122 (2019)
- G.H. Chen, F.F. Gu, M. Pan, L.Q. Yao, M. Li, X. Chen, Y. Yang, T. Yang, C.L. Yuan, C.R. Zhou, *J. Mater. Sci.: Mater. Electron.* **26**, 6511 (2015)
- A. Moulson, J. Herbert, *Electroceramics*, 2nd edn. (Wiley, London, 2003)
- M. Mousavi-Kamazani, *J. Mater. Sci.: Mater. Electron.* **30**, 17735 (2019)
- A.W. Sleight, W.J. Linn, *Ann. N. Y. Acad. Sci.* **272**, 22 (1976)
- D. Zhou, C.A. Randall, H. Wang, L.-X. Pang, X. Yao, *J. Am. Ceram. Soc.* **93**, 2147 (2010)
- R.G.M. Oliveira, D.B. Freitas, G.S. Batista, J.E.V. de Morais, V.C. Martins, M.M. Costa, M.A.S. Silva, D.X. Gouvêa, C. Singh, A.S.B. Sombra, *J. Mater. Sci.: Mater. Electron.* **29**, 16248 (2018)
- M. Valant, D. Suvorov, *J. Am. Ceram. Soc.* **83**, 2721 (2004)
- J. Yu, A. Kudo, *Adv. Funct. Mater.* **16**, 2163 (2006)
- P. Pookmanee, S. Kojinok, S. Phanichphant, *J. Met. Mater. Miner.* **22**, 49 (2012)
- M. Mousavi-Kamazani, *J. Alloys Compd.* **823**, 153786 (2020)
- D. Zhou, L.-X. Pang, J. Guo, H. Wang, X. Yao, C. Randall, *Inorg. Chem.* **50**, 12733 (2011)
- S. Sarkar, K.K. Chattopadhyay, *Physica E* **44**, 1742 (2012)
- Q. Sun, G. Li, T. Tian, Z. Man, L. Zheng, M. Barré, J. Dittmer, F. Goutenoire, A.H. Kassiba, *J. Eur. Ceram. Soc.* **40**, 349 (2020)
- M.A.S. Silva, R.G.M. Oliveira, A.S.B. Sombra, *Ceram. Int.* **46**, 20446 (2019)
- B. Ghosh, A. Dutta, T.P. Sinha, *J. Alloys Compd.* **554**, 80 (2013)
- P. Hollins, *Spectrochim. Acta A* **44**, 853 (1988)
- Y. Zhang, T. Tong, W. Kinsman, P. Jiang, G. Yin, S. Li, *J. Alloys Compd.* **549**, 358 (2013)
- R.N. Bhowmik, I. Panneer Muthuselvam, *J. Magn. Mater.* **335**, 64 (2013)
- H.M. Rietveld, *Acta Crystallogr.* **22**, 151 (1967)
- L. Bleicher, J.M. Sasaki, C.O. Paiva Santos, *J. Appl. Crystallogr.* **33**, 1189 (2000)
- A. El Yacoubi, A. Massit, S. El Moutaouikel, A. Rezzouk, B. Chafik El Idrissi, *Am. J. Mater. Sci. Eng.* **5**, 1 (2017)
- R.A. Young, A. Sakthivel, T.S. Moss, C.O. Paiva-Santos, *J. Appl. Crystallogr.* **28**, 366 (1995)
- C. Pascoal, R. Machado, V.C. Pandolfelli, *Cerâmica* **48**, 61 (2002)
- J.P.C. do Nascimento, A.J.M. Sales, D.G. Sousa, M.A.S. da Silva, S.G.C. Moreira, K. Pavani, M.J. Soares, M.P.F. Graça, J. Suresh Kumar, A.S.B. Sombra, *RSC Adv.* **6**, 68160 (2016)
- C. Pascoal, V.C. Pandolfelli, *Cerâmica* **46**, 76 (2000)
- J.R. MacDonald, *Appl. Opt.* **28**, 1083 (1989)
- R.G.M. Oliveira, M.C. Romeu, M.M. Costa, P.M. Silva, J.M.S. Filho, C.C.M. Junqueira, A.S.B. Sombra, *J. Alloys Compd.* **584**, 295 (2014)
- R.G.M. Oliveira, J.W.O. Bezerra, J.E.V. de Morais, M.A.S. Silva, J.C. Goes, M.M. Costa, A.S.B. Sombra, *Mater. Lett.* **205**, 67 (2017)
- K. Lily Kumari, K. Prasad, R.N.P. Choudhary, *J. Alloys Compd.* **453**, 325 (2008)
- I.I. Popov, R.R. Nigmatullin, A.A. Khamzin, I.V. Lounev, *J. Phys: Conf. Ser.* **394**, 012026 (2012)
- A.K. Jonscher, *J. Phys. D* **32**, R57 (1999)
- A.K. Jonscher, *J. Mater. Sci.* **13**, 553 (1978)
- M. Shah, M. Nadeem, M. Idrees, M. Atif, M.J. Akhtar, *J. Magn. Mater.* **332**, 61 (2013)
- C. Rayssi, F.I.H. Rhouma, J. Dhahri, K. Khirouni, M. Zaidi, H. Belmabrouk, *Appl. Phys. A* **123**, 778 (2017)

41. T. Lu, *Solid State Ionics* **21**, 339 (1986)
42. A. Zhang, J. Zhang, N. Cui, X. Tie, Y. An, L. Li, *J. Mol. Catal. A* **304**, 28 (2009)
43. M.M. Costa, G.F.M. Pires, A.J. Terezo, M.P.F. Graça, A.S.B. Sombra, *J. Appl. Phys.* **110**, 034107 (2011)
44. M. Ram, *Appl. Phys. A* **99**, 437 (2010)
45. Z.-L. Hou, M.-S. Cao, J. Yuan, X.-Y. Fang, X.-L. Shi, *J. Appl. Phys.* **105**, 076103 (2009)
46. M.-S. Cao, W.-L. Song, Z.-L. Hou, B. Wen, J. Yuan, *Carbon* **48**, 788 (2010)
47. M.-S. Cao, Z.-L. Hou, J. Yuan, L.-T. Xiong, X.-L. Shi, *J. Appl. Phys.* **105**, 106102 (2009)
48. R.G.M. Oliveira, G.S. Batista, J.E.V. de Moraes, M.M. Costa, M.A.S. Silva, J.W.O. Bezerra, A.S.B. Sombra, *J. Mater. Sci.: Mater. Electron.* **26**, 6511 (2018)
49. B. Lee, I. Abothu, P. Raj, C. Yoon, R. Tummala, *Scr. Mater.* **54**, 1231 (2006)
50. K. Hirota, G. Komatsu, M. Yamashita, H. Takemura, O. Yamaguchi, *Mater. Res. Bull.* **27**, 823 (1992)
51. X.-Z. Yuan, C. Song, W. Haijiang, J. Zhang, *Electrochemical Impedance Spectroscopy in PEM Fuel Cells. Fundamentals and Applications* (Springer, London, 2010)
52. J.R. MacDonald, *Impedance Spectroscopy* (Wiley, New York, 1987)
53. H. Rahmouni, M. Nouri, R. Jemai, N. Kallel, F. Rzigua, A. Selmi, K. Khirouni, S. Alaya, *J. Magn. Magn. Mater.* **316**, 23 (2007)
54. K.S. Cole, *J. Chem. Phys.* **10**, 98 (1942)

Publisher's Note Springer Nature remains neutral with regard to jurisdictional claims in published maps and institutional affiliations.